THE ASTROPHYSICAL JOURNAL, 473:929–945, 1996 December 20

THE MOLECULAR CORE ASSOCIATED WITH HH 25–26: CONTRACTION OR EXPANSION?

LOURDES VERDES-MONTENEGRO[1] AND PAUL T. P. HO[2]
Received 1995 August 1; accepted 1996 June 26

ABSTRACT

We mapped the star formation region HH 25–26 IR in the $NH_3(1, 1)$ and (2, 2) transitions using the VLA in its D configuration. The study has been made with 5″ angular resolution and 0.3 km s^{-1} velocity resolution.

As has been seen before, there is an elongated NH_3 core that lies perpendicular to the molecular outflow as traced in high-velocity CO emission. In this experiment, the NH_3 core is resolved, showing a central cavity and a number of distinct velocity features. Heating is seen at the position where the velocity features overlap spatially, and on the edges of the cavity, which is also seen as a reflection nebula with evidence for shock excitation. We have also detected what appears to be a new 1.3 cm continuum source on the wall of the cavity, associated with a 2.2 μm point source and jetlike structure. It is not clear at this time whether this is a truly continuum emission or high-velocity ammonia emission. The overall kinematics is complicated. A velocity gradient can be seen, together with the signatures for expanding or contracting motions.

We consider here two possible models: (*a*) a disk or ring structure, slowly rotating and contracting, and (*b*) an expanding cavity.

Subject headings: ISM: clouds — ISM: individual (HH 25–26) — ISM: jets and outflows — ISM: molecules — stars: pre–main-sequence

1. INTRODUCTION

HH 25–26 are a pair of Herbig-Haro objects located in the southern part of the star-forming complex NGC 2068, in the Orion molecular cloud L1630, at a distance of 460 pc. It is one of the few HH systems in which the ambient gas morphology remains perpendicular to the bipolar molecular outflow even at high angular resolutions. Therefore, it is a remarkable case for studying confinement structures. The Herbig Haro objects were studied in the optical by Strom et al. (1986). In their CCD images, HH 25, as well as their nebulous objects S2, S3, and S6, is seen predominantly via reflection. HH 26, on the other hand, has a weak emission component and is quite prominent in the [S II] frames. S4 and S5 seem to be shocked nebulous objects as deduced from a comparison of the *I* and *R* images from Strom et al. (1986). Two extended *IRAS* sources exist in the area. In addition, Strom, Strom, & Vrba (1976) identified a 2.2 μm source number 59 in their list.

In a later study by Cohen & Schwartz (1983), a point source was also found in the same region, 30″ NE of SSV 59. In their study, and also in a subsequent paper by Reipurth et al. (1993), the point source appears erroneously to refer to the extended SSV 59. Therefore, we adopt a position for the point source as measured in Figure 13 of Cohen & Schwartz and for SSV 59 as in the original paper by Strom et al. (1976). A continuum source has been detected at 3.6 cm by Anglada et al. (1995) at nearly 10″ to the southeast of HH 25.

A low-collimation molecular outflow was also detected and mapped by Snell & Edwards (1982) in the CO(1–0) and CO(2–1) lines with an angular resolution of 50″ and 1.′3, respectively. Gibb & Heaton (1993), with a higher angular resolution (22″) in the CO(2–1) line, have recently resolved the outflow into several lobes.

The ambient high-density gas has been studied in the CS(1–0) transition by Pastor et al. (1991) and in the CS(2–1) and CS(5–4) and HCO^+(4–3) lines by Gibb & Heaton (1993). Single-dish NH_3 studies have also been made by Matthews & Little (1983) (beam ∼2.′2), Torrelles et al. (1983) (beam ∼1.′5), and Menten, Walmsley, & Mauersberger (1987) (beam ∼40″). The structures were found to be elongated in the same direction as the HH 25–HH 26 pair and to be perpendicular to the CO molecular outflow. Torrelles et al. (1983) detected a velocity gradient of ∼0.5 km s^{-1} pc^{-1} along the major axis of the structure, and they suggested that the observed condensation was an interstellar toroid that may collimate the bipolar outflow. With the VLA in its D configuration, they found further that the NH_3 emission associated with HH 25 and HH 26 seems to be a flattened structure (Torrelles et al. 1989). This structure is perpendicular to the CO bipolar outflow and appears to be doubly peaked with 15″ resolution. This appears consistent with a toroid possibly collimating the outflow. However, the VLA experiment did not detect the velocity gradient observed in the single-dish measurements by Torrelles et al. (1983), due to the low signal-to-noise ratio and a relatively coarse velocity resolution (1.2 km s^{-1}). In Figure 1 we show all the objects present in the field, together with the molecular outflow mapped in CO(2–1) by Gibb & Heaton (1993) and the VLA-NH_3 structure found by Torrelles et al. (1989). The positions of the objects are listed in Table 1.

Here we present new $NH_3(1, 1)$ and (2, 2) observations using the VLA in its D configuration with the improved *K*-band receivers. We used a new phase center midway between HH 25 and HH 26, a velocity resolution of 0.3 km s^{-1}, and an angular resolution of ∼5″, achieving a sensitivity of ∼5 mJy beam^{-1}. The improvement in sensitivity relative to the previous observations by a factor of

[1] Instituto de Astrofísica de Andalucía, CSIC, Apdo. 3004, 18080 Granada, Spain.
[2] Harvard-Smithsonian Center for Astrophysics, Cambridge, MA.

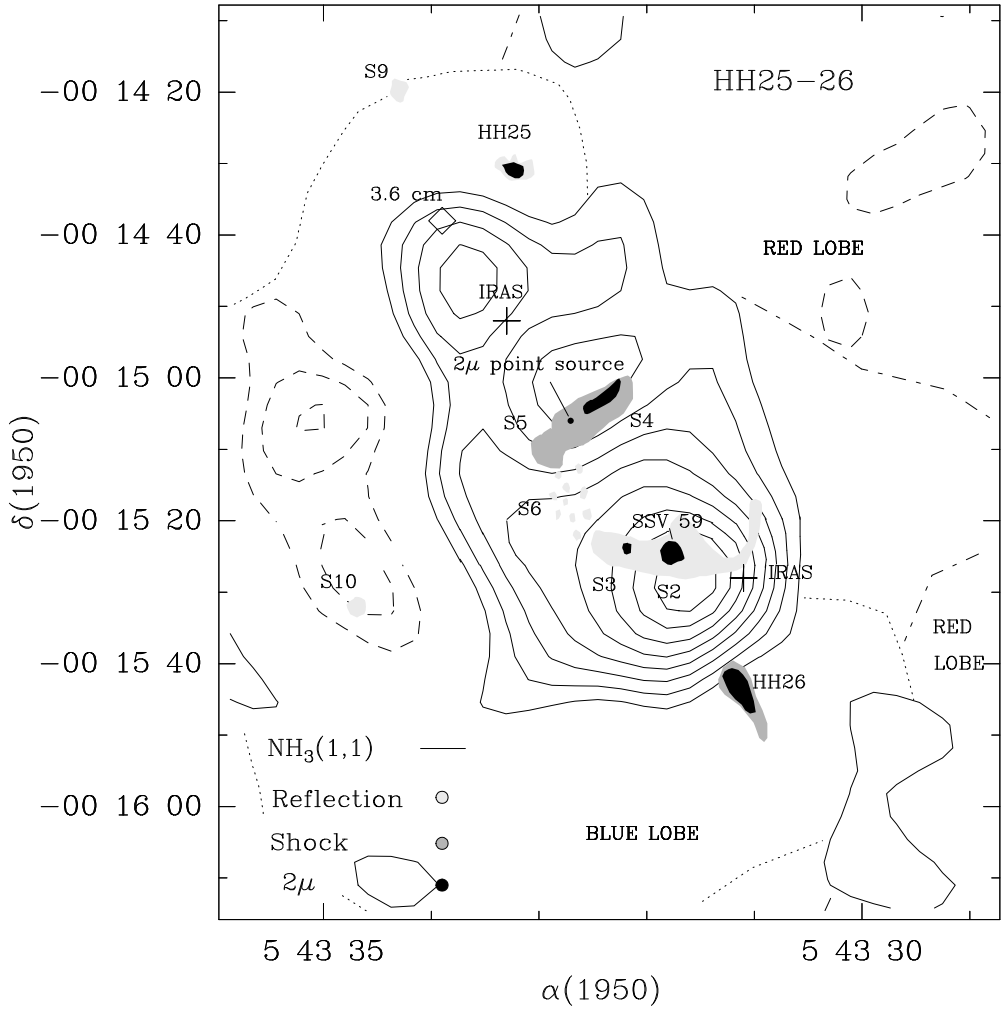

FIG. 1.—Fig. 1 of Torrelles et al. (1989) [contour map of the (1, 1) ammonia main transition at the (V_{LSR}) = (9.7, 10.9) km s^{-1} range in velocity]. We have plotted the main knots of near infrared emission reported in Fig. 26 from Strom et al. (1986). The darkest knots are due mainly to reflection, and the lighter knots have a shocked component. The 2.2 μm emission, taken from Cohen & Schwartz (1983), has also been plotted as a black area. The positions and references for all the objects plotted in the field are given in Table 1. The outer contours of the red and blue lobe of the molecular outflow mapped in CO(2–1) by Gibb & Heaton (1993) are also plotted as dashed lines.

TABLE 1

OBJECTS IN THE FIELD

Objects	Positions[a]	Symbol[b]	Reference
IRAS source	05 43 31.1, −00 15 28.0	+	1
HH 26	05 43 31.2, −00 15 42.0	△	2
2 μm[c]	05 43 32.6, −00 15 07.0	+	3
SSV 59	05 43 31.6, −00 15 23.0	+	4
S2	05 43 31.8, −00 15 24.5	*	2
S3	05 43 32.2, −00 15 23.4	*	2
S4	05 43 32.3, −00 15 03.0	*	2
1.3 cm continuum	05 43 32.7, −00 15 06.0	◇	5
S6	05 43 32.8, −00 15 19.0	*	2
S5	05 43 32.9, −00 15 10.0	*	2
HH 25	05 43 33.2, −00 14 31.0	△	2
IRAS source	05 43 33.3, −00 14 52.0	+	1
S9	05 43 34.3, −00 14 20.0	*	2
S10	05 43 34.7, −00 15 32.0	*	2
3.6 cm continuum	05 43 33.9, −00 14 38.0	◇	6

[a] Listed are right ascension, in units of hours, minutes, and seconds, and declination, in units of degrees, arcminutes, and arcseconds.

[b] These symbols are used to represent these objects in the accompanying figures.

[c] Obtained by the authors from Fig. 13 of Cohen & Schwartz 1983.

REFERENCES.—(1) *IRAS* catalog. (2) Strom et al. 1986. (3) Cohen & Schwartz 1983. (4) Strom et al. 1976. (5) This paper. (6) Anglada et al. 1994.

~ 10 allows a better definition of the interaction of the dense gas and the molecular outflow in terms of morphology, kinematics, and heating. This made it possible to constrain the location of the exciting source of the outflow.

2. SYSTEM PARAMETERS AND DATA ANALYSIS

Observations of HH 25–26 were made using the VLA of the NRAO (National Radio Astronomy Observatory)[3] in the D configuration during 1992 July 18. The $(J, K) = (1, 1)$ and (2, 2) lines of NH_3 ($\lambda \sim 1.3$ cm) were observed simultaneously with both polarizations under good weather conditions. The spectrometer covered the main quadrupole hyperfine component for both lines and the inner satellites of the (1, 1) transition (see Ho & Townes 1983). We used 61 spectral channels with a spectral resolution of 24.4 kHz (~ 0.3 km s^{-1}) for a total bandwidth of 1.563 MHz for each line. The LSR velocity of the central spectral channel was 10.30 km s^{-1}. The primary flux calibrators were 1328+307 and 0134+329, for which we adopted a K-band flux of 2.44 Jy and 1.08 Jy, respectively. The phase calibrator was 0529+075, with a bootstrapped flux of 2.67 Jy. From phase noise, we estimated that our absolute positions are accurate to 5% of the synthesized beams. The phase center of the array was set at $\alpha(1950) = 05^h43^m32^s.7$, $\delta(1950) = -00°15'08''.0$. The primary beam size at full width half-maximum (FWHM) is $\sim 2'$ at $\lambda = 1.3$ cm.

Maps for individual spectral channels were made by Fourier transformation of the calibrated (u, v) visibility data, using the standard algorithms of the Astronomical Image Processing System (AIPS) from NRAO. We have removed the continuum contribution from the ammonia maps before further processing of the data. In order to do that, we have averaged the line free channels of the (2, 2) line in the (u, v) domain (the task AVSPC of AIPS has been used) with natural weighting and applied a Gaussian tapering function to the (u, v) data with a half-width at a 30% level of 40 kλ (beam size $5''.8 \times 5''.2$, P.A. $= -6°$). The resulting map has been subtracted from all the individual channels. The cleaned maps were obtained in two different ways: (*a*) the channel maps have been produced with natural weighting and the same Gaussian tapering function of 40 kλ (beam size $5''.8 \times 5''.2$, P.A. $= -6°$); (*b*) for further processing of the data, we have also used a Gaussian tapering function of 20 kλ and natural weighting (beam size $9''.0 \times 8''.5$, P.A. $= -5°$) in order to enhance our sensitivity to spatially extended low-brightness emission. The rms noise levels for these maps are 5.3 mJy and 7.7 mJy, respectively.

3. RESULTS

3.1. *Channel Maps and Integrated Emission*

In Figures 2*a* and *a*2*b* we display the channel maps of the NH_3(1, 1) and (2, 2) main hyperfine line emission at the observed radial velocities, with a channel width of 0.3 km s^{-1} and a synthesized beam of $\sim 5''$. We have marked the positions of the objects listed in Table 1. The inner satellite hyperfine lines of the (1, 1) transition were also detected in this experiment and have been used for the opacity calculations (see § 4.1).

[3] NRAO is operated by Associated Universities, Inc., under cooperative agreement with the National Science Foundation.

A comparison with our previous VLA observations of HH 25–26 in ammonia (Torrelles et al. 1989; Fig. 1) shows the considerable improvement in the definition of the dense gas distribution with higher sensitivity and higher angular and spectral resolutions. We have studied the NH_3(1, 1) and (2, 2) main hyperfine line emission with a channel width of 0.3 km s^{-1} and a synthesized beam of $\sim 5''$. The inner satellite hyperfine lines of the (1, 1) transition were also detected in this experiment and have been used for the opacity calculations (see § 4.1).

Three different clumps (hereafter HH 25–26 A, B, and C), very close in velocity, seem to be present at channels with V_{LSR} in the ranges 9.0–10.2 km s^{-1}, 10.2–11.1 km s^{-1}, and 11.1–11.7 km s^{-1}, respectively, although blending in velocity does not allow a complete isolation (see also position-velocity diagrams in § 3.3). Integration of the NH_3(1, 1) emission in the above-mentioned velocity ranges is shown in Figures 3*a*, 3*b*, and 3*c*, respectively. Note that the NH_3 emission for the second velocity range *surrounds the reflection nebula* observed by Strom et al. (1986). In particular, we have detected at $V_{LSR} = 10.9$ km s^{-1} an arc tracing the southern edge of the reflection nebula (Fig. 2*a*). There are some filamentary structures present. For example, there is a southeast extension immediately to the south of a gap in the integrated emission. This gap coincides with a weak reflection area (Fig. 1). Careful inspection of the individual spectra suggests that further decomposition of the velocity structures may be possible. However, the global changes are fairly well described by the three ranges mentioned above, and we will keep such a separation throughout the paper. Figure 4 shows the spectra toward three different directions. In Figure 4*a*, the line width is narrow and corresponds to HH 26B. In Figures 4*b* and 4*c*, the line width is broader and appears to be a blend of HH 25A, B, and C.

For an overall view of the NH_3 emission, we determined its integrated column density distribution. In Fig. 5*a* we show the sum of the integrated emission of the main hyperfine component of the (1, 1) and (2, 2) lines. The integrated emission of the NH_3(1, 1) and (2, 2) main lines are shown individually in Figures 5*b* and 5*c*, respectively. The (2, 2) line is weaker, but its structures are consistent with those in the (1, 1) line. In the paper by Torrelles et al. (1989), both peaks of the (1, 1) integrated emission have the same intensity after primary beam correction. Here both peaks are equidistant to the phase center, but the northern one is stronger. There is no contradiction, however, with previous results, since the southern emission is more extended than our present synthesized beam. When convolved with the 15″ resolution of the previous experiment, the total flux of the two condensations is comparable.

The CS (5–4) map made by Gibb & Heaton correlates well with our NH_3 map, except to the southeast of HH 25, where they find more gas. An inspection of the CS spectra and the velocity range used to produce the CS map suggests that high-velocity wing emission may have been included together with the ambient cloud emission. The blue lobe of the outflow is intense southeast of HH 25, and this could account for the observed difference between the CS and NH_3 maps.

3.2. *Continuum Emission*

We have detected what appears to be a new continuum source, located on the northeastern side of the cavity structure defined by the reflection and shocked nebula. To

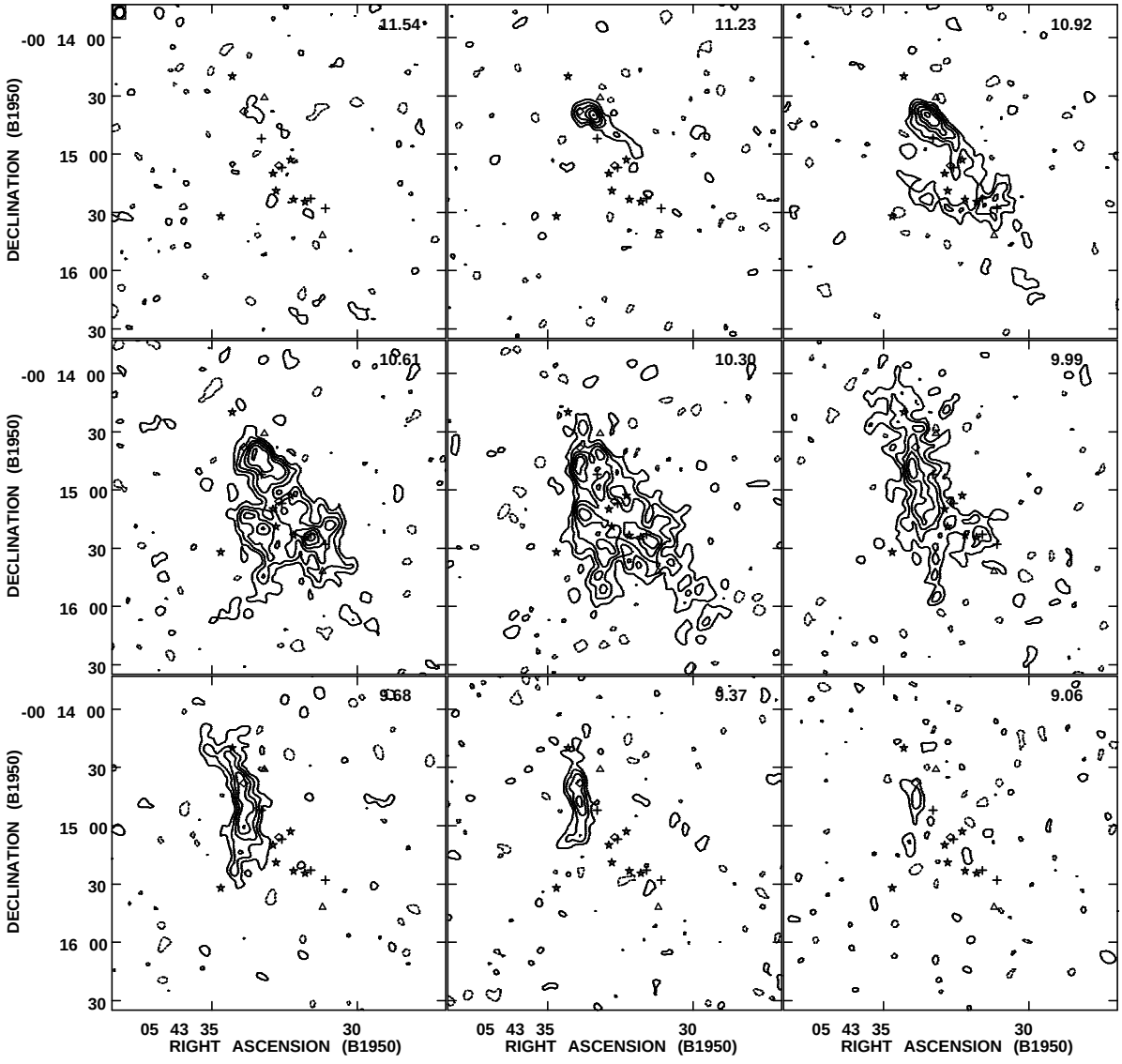

FIG. 2.—(*a*) Individual channel maps for the $NH_3(1, 1; m)$ emission (channel width ~ 0.3 km s^{-1}). The velocity for each channel is indicated. The contour levels are 5.3 mJy beam^{-1} × (−4, −2, 2, 4, 6, 8, 10 and 12), with 1 σ = 5.3 mJy beam^{-1}. Maps have been obtained after a 40 kλ Gaussian tapering (synthesized beam $\sim 5\farcs8 \times 5\farcs2$, P.A. = −6°). The continuum emission has been subtracted. The marked objects are listed in Table 1. (*b*) Same as (*a*) for the $NH_3(2, 2; m)$ line.

produce this continuum map, we have averaged the channel maps deemed to be free of line emission when made with a synthesized beam of $\sim 5''$ (Fig. 6) (see § 2). The peak emission has a value of 6 mJy (1 σ = 1.1 mJy), and the source appears to have underlying structure. This is, however, at a very weak level, so we have fitted a two-dimensional Gaussian to estimate its size and orientation. The fitted Gaussian is centered at $\alpha = 05^h43^m32\overset{s}{.}7 \pm 0.09$ and $\delta = -00°15'06\farcs1 \pm 0.65$. This position coincides with that of the 2.2 μm point source (see Table 1). Its size is $11\farcs1 \pm 1\farcs8 \times 9\farcs1 \pm 1\farcs1$,with a P.A. of $-45° \pm 45°$. Its deconvolved size is $9\farcs6 \pm 1\farcs7 \times 7\farcs3 \pm 1\farcs1$ and P.A. = 130° ± 40°.

Anglada et al. (1995) did not detect this source at λ = 3.6 cm at a 3 σ level of 0.1 mJy. There are three possible explanations: (1) the source has a spectral index larger than ~ 4, which could correspond to dust emission, (2) the source is variable, or (3) this is not continuum but high-velocity ammonia emission. In order to test this last possibility, we have compared the emission of the blueshifted and redshifted channels that compose the continuum map. We have averaged them independently, finding differences between them at very faint levels. If real, this could indicate that all or part of the "continuum emission" may be in fact high-velocity ammonia emission. This is not, however, conclusive, and we are planning a higher sensitivity and multiwavelength study in order to clarify the nature of the source.

3.3. *Kinematics*

In order to study the kinematics of the dense gas, we have calculated the intensity-weighted mean radial velocity, velocity dispersion, and selected position-velocity diagrams for the NH_3 emission.

In Figure 7 we present a gray-scale map of the intensity-weighted mean velocity as computed by taking the first-order moment of the main hyperfine component of the $NH_3(1, 1)$ line. It shows a velocity gradient both in the southeast-northwest direction and the northeast-southeast

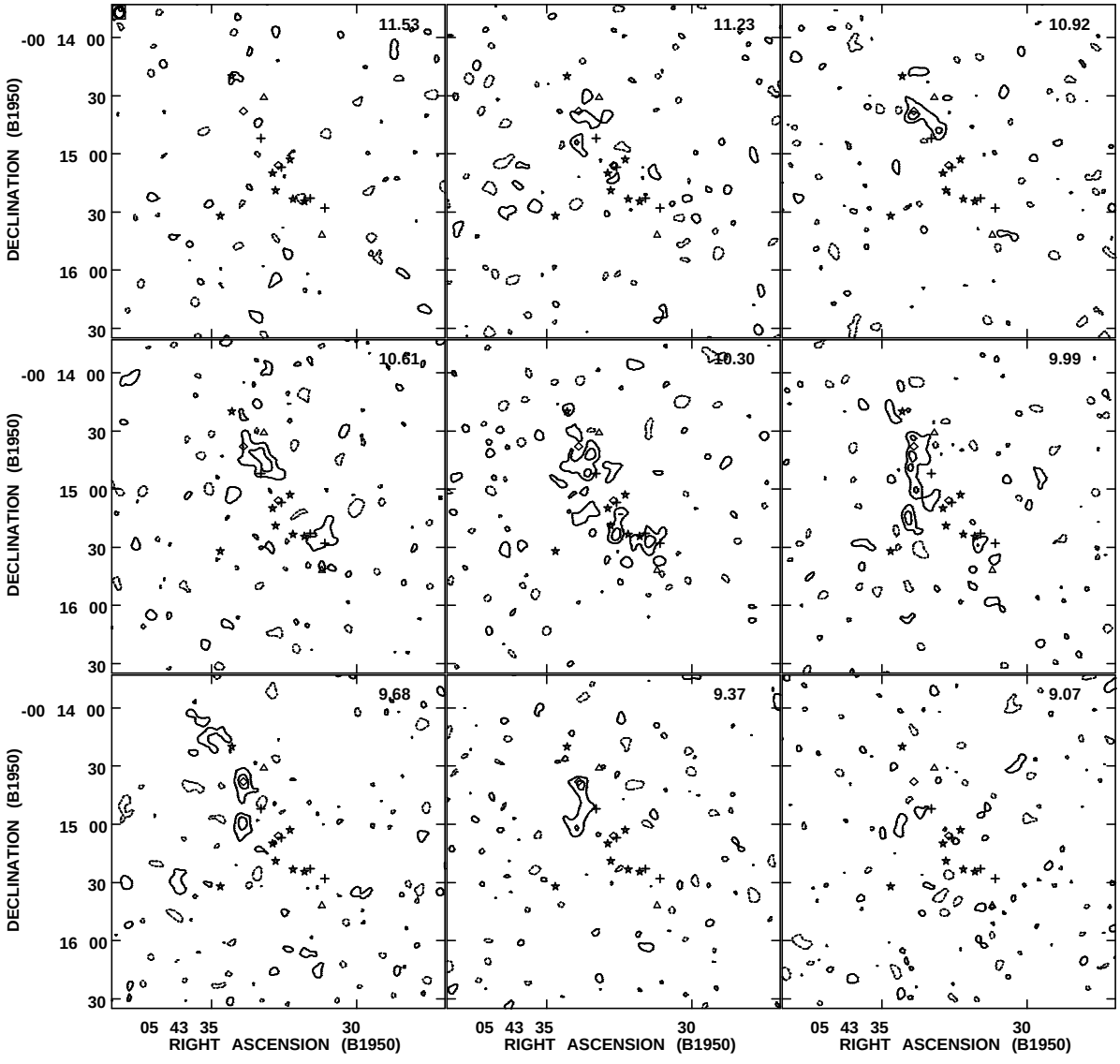

FIG. 2*b*

direction, going from $V_{LSR} = 9.8$ to 10.6 km s^{-1}. This gradient is in fact produced by the change of relative intensity of the different clumps. As shown in the position-velocity diagram of Figure 8*a* (made along the southeast-northeast direction as marked in Fig. 7), the component centered at $\sim$9.8 km s^{-1} (HH 25–26 A) dominates to the southeast, and the emission to the northwest is dominated by the component centered at $\sim$11.3 km s^{-1} (HH 25–26 C), together with a weaker one at $\sim$10.6 km s^{-1} (HH 25–26 B).

We have also produced two position-velocity diagrams along the walls of the cavity located in front of the 1.3 cm continuum source (north-south direction in Fig. 8*b* and east-west in Fig. 8*c*). Both diagrams show a C-shaped variation in velocity, a signature of expansion or contraction. The velocity of the main component in Figure 8*b* (HH 25–26 B) decreases from 10.6 km s^{-1} to 10.0 km s^{-1} and increases up to the previous value of 10.6 km s^{-1} from north to south. There is also some gas at 9.8 km s^{-1} (HH 25–26 A) and 11.3 km s^{-1} (HH 25–26 C), as marked in the figure. The emission of HH 25–26 B dominates also in the diagram of Figure 8*c*, with velocities decreasing from 10.7 km s^{-1} to 10.3 km s^{-1} and increasing again up to 10.7 km s^{-1}, from east to west. Some emission of HH 25–26 A ($V_{LSR} \sim 10.3$ km s^{-1}) is also present.

The second moment of the emission shows two peaks, coincident with the areas in which the different velocity components overlap. Therefore, these maxima are not indicating a line width enhancement. For this reason, we have looked at the individual spectra, finding typical line widths of the individual components of 0.6–1.0 km s^{-1}.

4. PARAMETERS OF THE NH_3 EMISSION

4.1. *Opacity*

In order to derive the optical depth of the main line emission, we have used the approximate equivalence $\int S_\nu(1, \quad 1; is)\,dV / \int S_\nu(1, \quad 1; m)\,dV \sim (1 - e^{-\tau(1,1;m)})/(1 - e^{-\tau(1,1;m)\times 0.28})$ (Ho & Townes 1983), which is only exact when the main and satellite components have the same line width. Since our ammonia observations include both the main and the inner satellite hyperfine components of the (1, 1) transition, we have been able to make an opacity map, shown in a gray scale in Figure 9.

Significant opacity changes are present in the conden-

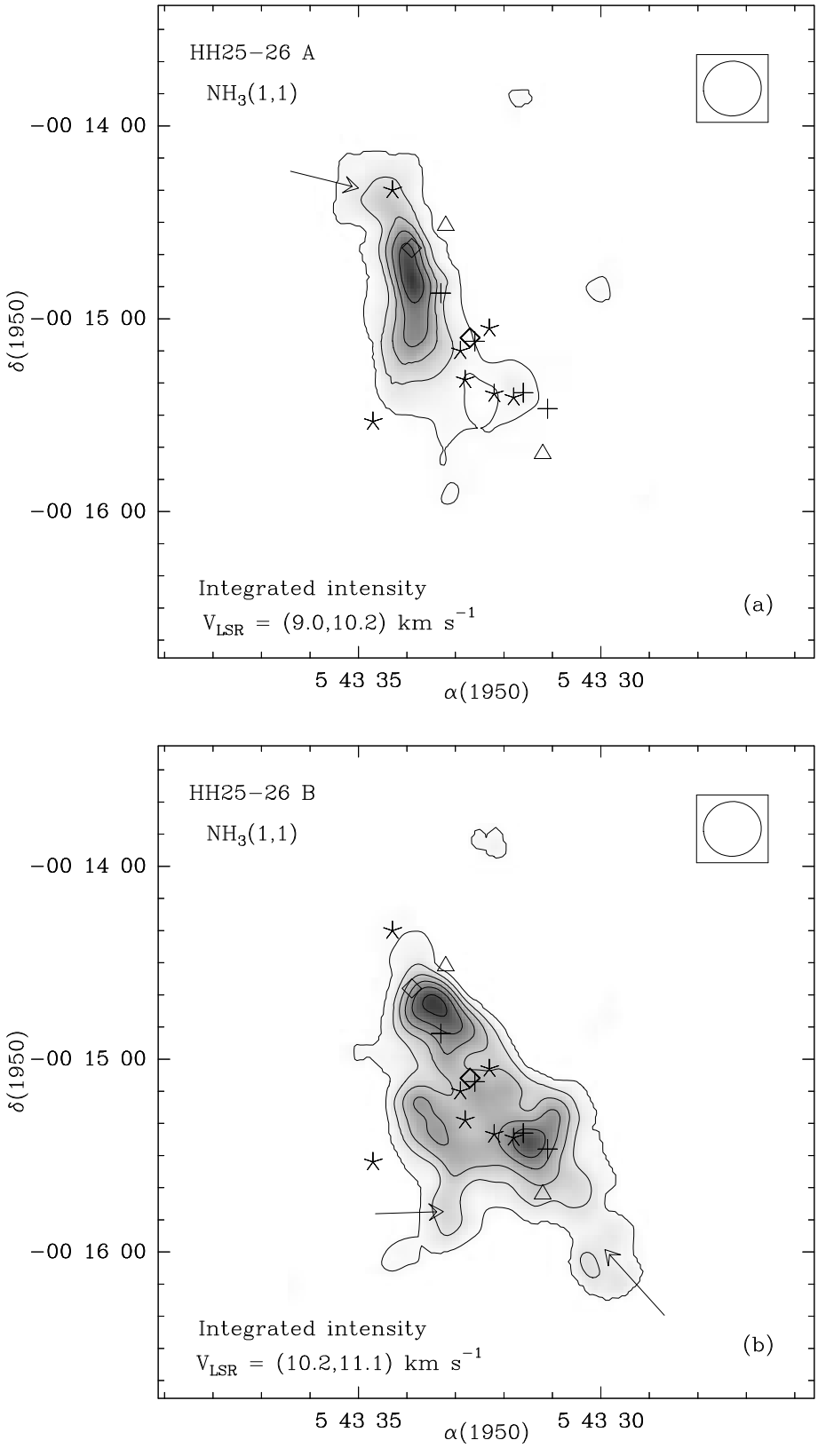

FIG. 3.—(*a*) Integrated emission map of the $NH_3(1, 1; m)$ emission in the velocity range corresponding to the eastern condensation (HH 25–26 A), $(V_{LSR}/\text{km s}^{-1}) = (9.0, 10.2)$ km s^{-1} in a contour and gray-scale representation. The map has been obtained after a 20 kλ Gaussian tapering (synthesized beam $\sim 9''.0 \times 8''.5$, P.A. $= -5°$). The continuum emission has been subtracted. The objects are listed in Table 1. The arrow marks the filamentary structure mentioned in § 3.1. The plotted levels are 7.5, 30, 52.5, 75, and 97.5 mJy km s^{-1}. (*b*) Same as (*a*), but for the $NH_3(1, 1; m)$ emission in the velocity range corresponding to the western condensation (HH 25–26 B), $(V_{LSR}/\text{km s}^{-1}) = (10.2, 11.1)$ km s^{-1}. The arrows mark the filamentary structures mentioned in § 3.1. The plotted levels are 10, 30, 50, 70, 90, and 110 mJy km s^{-1}. (*c*) Same as (*a*), but for the $(1, 1; m)$ emission in the velocity range corresponding to the northern clump (HH 25–26 C), $(V_{LSR}/\text{km s}^{-1}) = (11.1, 11.7)$ km s^{-1}. The plotted levels are 5, 15, 25, and 35 mJy km s^{-1}.

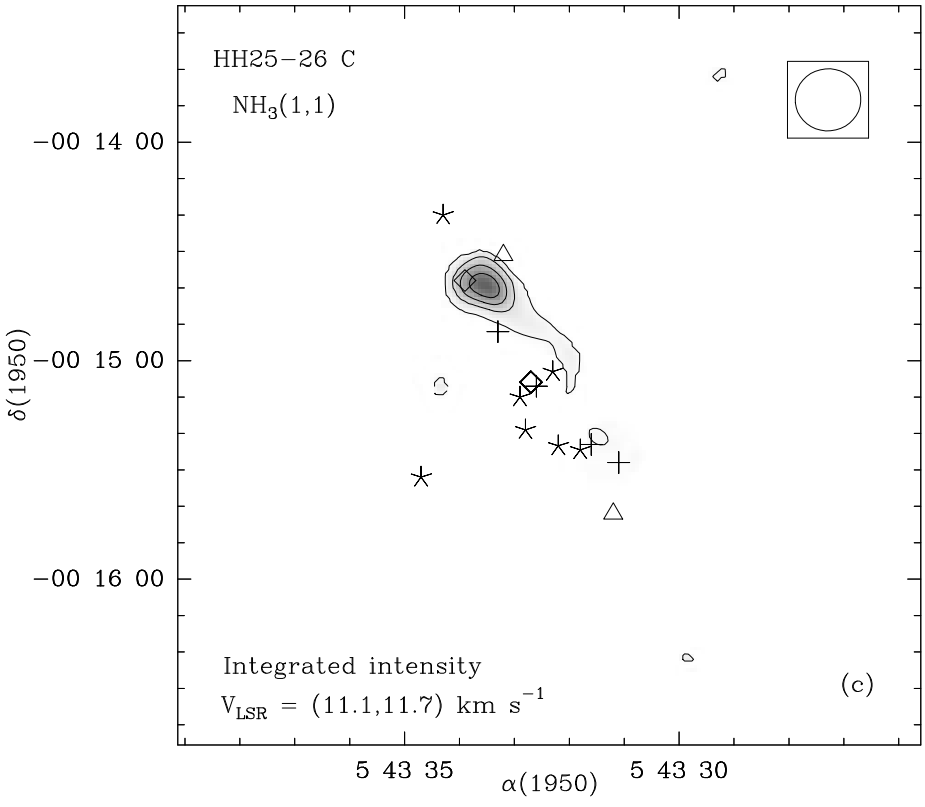

FIG. 3.—*Continued*

sations ($\tau \sim 0.1$–2.5). For the areas in which these changes are not due to edge effects, we have calculated the corresponding typical opacity values from Gaussian fits to the spectra. The separation of the different velocity components is not possible for the satellite lines at most of the positions, so that mean opacities have been estimated there. The differences between the fitted values and the ones shown in the map are due to the overlapping of the different velocity components, and the agreement is within a 20% level. The opacity enhancments observed by Torrelles et al. (1989) are resolved here: their northern and southern areas are composed here of three and two subareas, respectively, with peak opacities as marked in Figure 9.

4.2. *Heating of the* NH_3 *Structure*

Variations in the ratio of the integrated intensities of the (2, 2; *m*) and (1, 1; *m*) lines correspond to variations in the rotational temperature (assuming constant opacity and the same linewidth for the (1, 1; *m*) and (2, 2; *m*) lines. The rotational temperature between the (2, 2; *m*) and the (1, 1; *m*) states of the ammonia molecule is a good indicator of the kinetic temperature for low temperature regimes (Ho & Townes 1983). For gas kinetic temperatures $T_K > 40$ K, $T_{\rm rot}(2, 2; 1, 1)$ underestimates T_K, since the higher energy rotational states become more important (Walmsley & Ungerechts 1983; Danby et al. 1988).

We have obtained the ratio $\int S_\nu(2, 2; m)\, dV / \int S_\nu(1, 1; m)\, dV$ separately for the three velocity ranges corresponding to HH 25–26 A, B, and C. In order to exclude edge effects and to make a quantitative estimation of the rotational temperature, we have inspected the $NH_3(1, 1)$ and (2, 2) spectra and fitted Gaussians to them where the separation of the three velocity components has been feasible. The results are listed in Table 2 for HH 25–26 A and B. The weakness of component C, together with its blending with component B, prevents accurate fitting to the spectra. Therefore, the values given in Table 2 for HH 25–26 C are only estimated ones. Selected spectra are shown in Figure 10, where the change in relative intensity between the $NH_3(1, 1)$ and (2, 2) lines can be seen.

This ratio increases for the common edges of the three NH_3 clumps, as can be seen in Figure 10*a*–10*c*, and rotational temperatures are enhanced there up to 20–35 K (see Table 2). The map obtained for HH 25–26 A shows two other peaks (Fig. 10*a*). The one located to the east seems to be real, since there is integrated $NH_3(2, 2)$ emission associated there, as can be seen in Figure 5*c*. However, it cannot be seen above the rms level in the spectra, and therefore a heating effect cannot be concluded. The peak to the southwest is an edge effect. The rotational temperature is also enhanced along the edges of the cavity in HH 25–26 B (Fig. 10*b*). The achieved rotational temperature there is of the order of 30 K (see Table 2).

4.3. *Masses*

The parameters of the ammonia condensations are presented in Table 3. The calculations have been made as explained in the footnotes of that table. As can be seen there, HH 25–26 B has been separated into three subclumps, named B1, B2, and B3, the reason being only geometrical. The total mass of HH 25–26 A, B, and C is ~ 7 $M_\odot \times \{[(NH_3)/(H_2)]/10^{-8}\}$, with 70% in HH 25–26 B. The mass seen with single-dish observations is calculated to be larger than 70 $M_\odot$ by Matthews & Little (1983). The integrated flux in the (1, 1; *m*) line of the VLA ammonia structure is ~ 4 Jy km s^{-1} within an area of 0.35 arcmin^2. This is

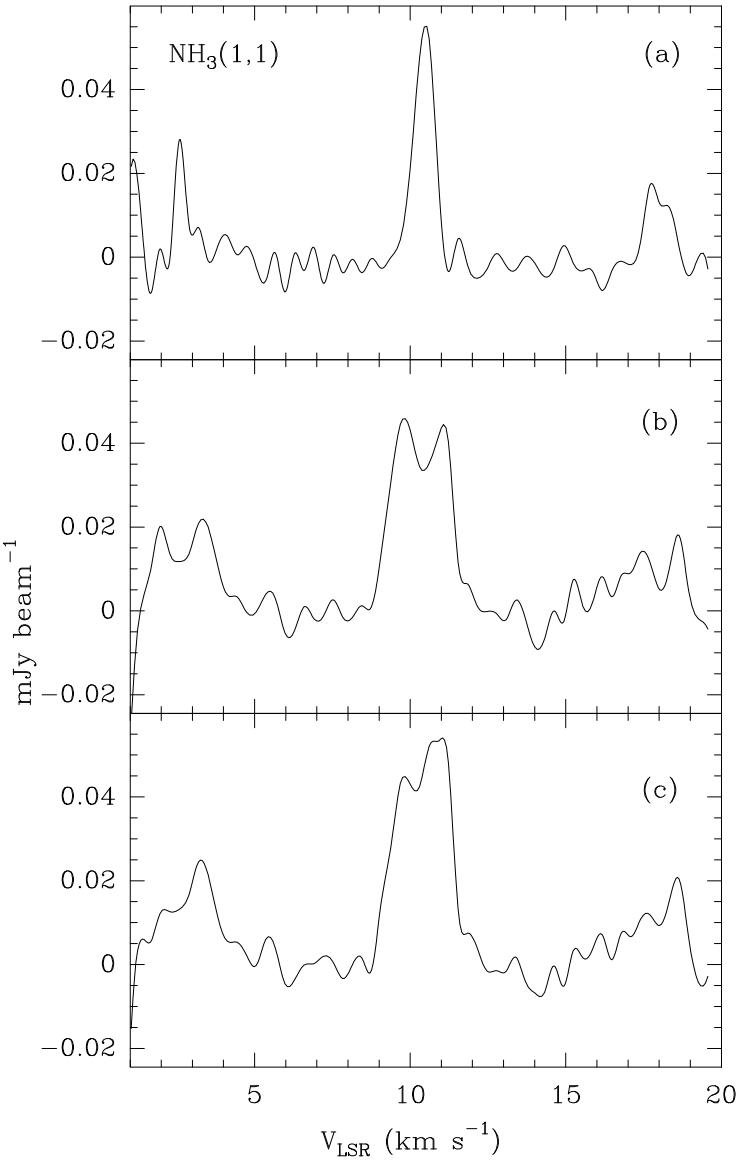

FIG. 4.—Spectra of the inversion line $(J, K) = (1, 1)$ of NH_3, observed toward (*a*) $\alpha(1950) = 05^h43^m33^s.8$, $\delta(1950) = -00°14'39''.1$. (*b*) $\alpha(1950) = 05^h43^m33^s.3$, $\delta(1950) = -0°15'25''.0$. (*c*) $\alpha(1950) = 05^h43^m33^s.8$, $\delta(1950) = -00°14'36''.8$. The primary beam size at FWHM is $\sim 5''.8 \times 5''.2$, with P.A. of $-6°$.

an $\sim 20\%$ of the flux seen with single-dish observations (Matthews & Little 1983; Torrelles et al. 1993). The lower values obtained here with interferometric observations for mass and flux indicate that a significant amount of extended molecular gas is missing in our map.

5. DISCUSSION AND CONCLUSIONS

There are a number of important clues that need to be incorporated in any viable model: (1) a number of velocity features are apparent, (2) there seems to be a central exciting source as suggested by the 2 μm jetlike structure, and the 1.3 cm continuum source that could be high due to high-velocity ammonia emission, (3) a molecular outflow that is more or less perpendicular to the elongated NH_3 core, (4) heating is seen in the center and also where the velocity features overlap spatially, (5) Herbig-Haro objects are perpendicular to the molecular outflow and are at the edges of the NH_3 core, and (6) opacity measurements suggest the formation of density peaks within the NH_3 core. We will try to explain these features in the context of two working models.

5.1. *A Disk or Ring Structure*

In our previous VLA study (Torrelles et al. 1989), we suggested that HH 25–26 could be a good candidate for an interstellar toroid, since the gas was distributed in a flattened structure perpendicular to the bipolar molecular outflow. However, since the emission was detected only in a single spectral channel, we could not confirm a gradient of 0.5 km s^{-1} pc^{-1} as seen with the single dish. In this experiment, with 0.3 km s^{-1} resolution, emission is detected over nine spectral channels. An overall velocity gradient can be seen in our maps (e.g., Fig. 7), but the overall kinematics appears to be more complicated. A number of separate velocity features are seen, and the apparent velocity gradient seems to be the result of the superposition of these features. Is a toroidal model still viable? The presence of multiple velocity components is at first glance problemati-

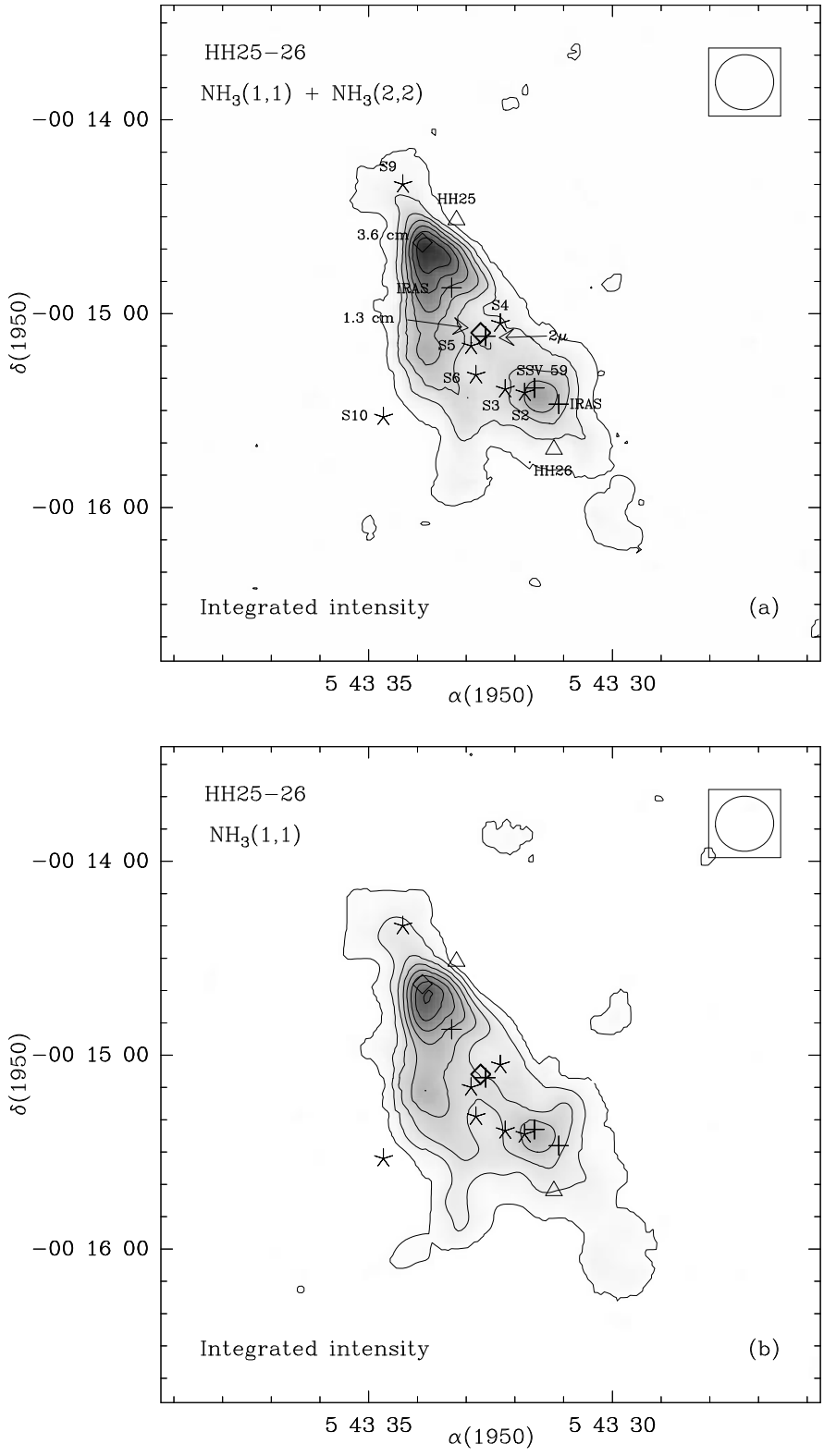

FIG. 5.—(*a*) Integrated emission map in a contour and gray-scale representation corresponding to the main line plus inner satellites of $NH_3(1, 1)$ added to the $NH_3(2, 2)$ main line emission in the velocity range V_{LSR}/km s^{-1} = (1.7, 18.9). The map has been obtained after a 20 kλ Gaussian tapering (synthesized beam $\sim 9''.0 \times 8''.5$, P.A. $= -5°$). The continuum emission has been subtracted. The marked objects are listed in Table 1. Contour levels are 20, 80, 140, 200, 260, 320, and 380 mJy km s^{-1}. (*b*) Same as (*a*), but for the $NH_3(1, 1; m)$ line emission, with levels 10, 40, 70, 100, 130, 160, 190, and 220 mJy km s^{-1}. (*c*) Same as (*a*), but for the $NH_3(2, 2; m)$ line emission, with levels 11, 44, and 77 mJy km s^{-1}.

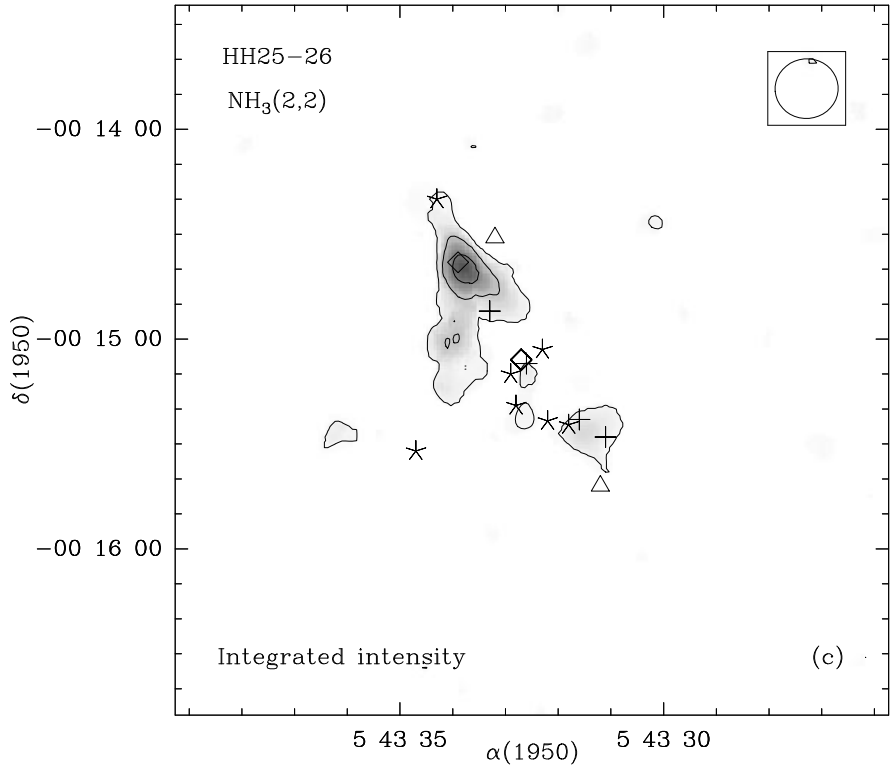

FIG. 5.—*Continued*

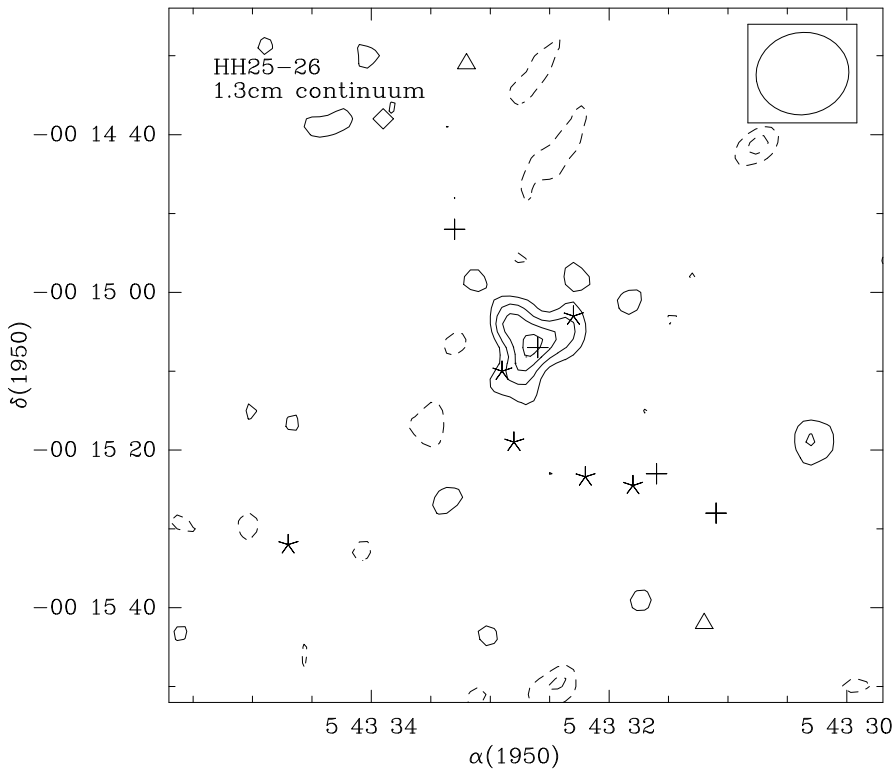

FIG. 6.—The 1.3 cm radio continuum source that we have detected toward $\alpha(1950) = 05^h43^m32^s.7$ and $\delta(1950) = -00°15'06''.1$. The map has been produced with natural weighting and an HPBW for the Gaussian tapering function of 40 kλ (beam size $5''.8 \times 5''.2$, P.A. $= -6°$). The contours are -3.3, -2.2, 2.2, 3.3, 4.5, and 5.5 mJy. The rms is about 1 mJy. The marked objects are listed in Table 1.

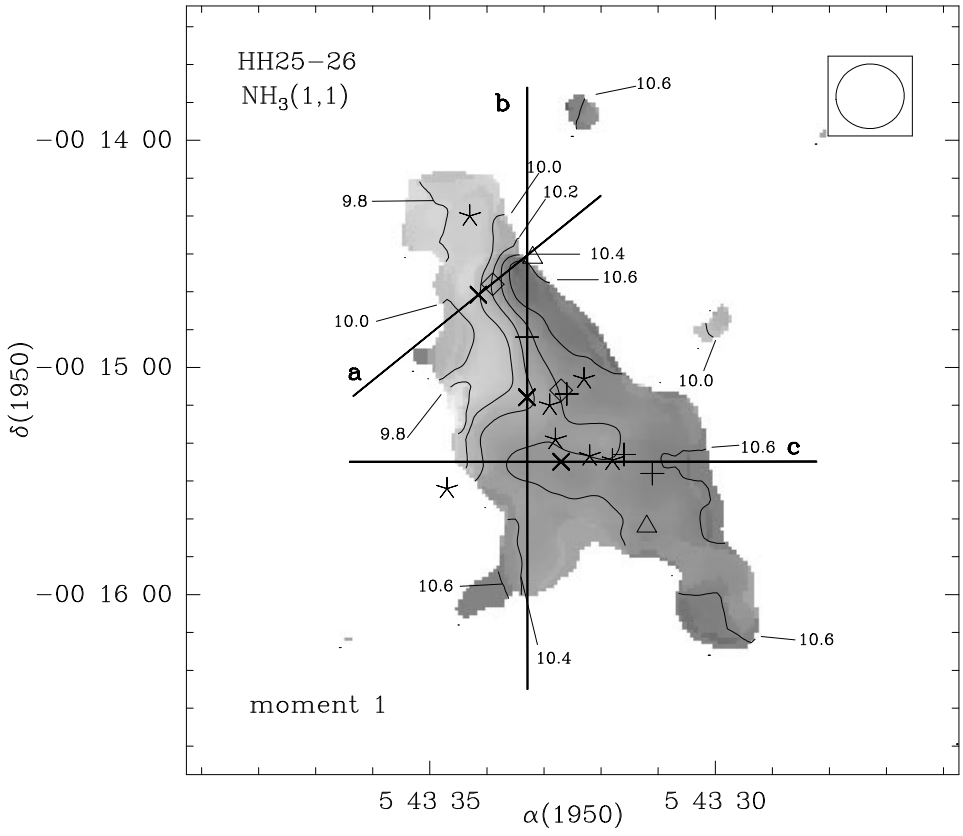

FIG. 7.—First-order moment map of the (1, 1; *m*) line calculated in the velocity range V_{LSR} = (8.4, 11.8) km s^{-1}. The contours range from 9.8 to 10.6 km s^{-1} with a step of 0.2 km s^{-1}, as numbered in the figure. The gray scale is linear. The map has been obtained after a 20 kλ Gaussian tapering (synthesized beam $\sim$9.″0 × 8.″5, P.A. = −5°), and the continuum has been subtracted. The lines indicate the directions for the position-velocity diagrams in Fig. 8, and the crosses on them indicate the reference position for those diagrams.

cal. However, the spatial proximity and the small velocity dispersion suggest that the different velocity features could still be a coherent structure. The presence of distinct peaks in the spatial distribution of line opacity (and therefore column density) suggests a clumpy or fragmented core. Furthermore, the binding mass for this structure (0.5 km s^{-1} over a 0.1 pc scale) is 5 $M_\odot$, which is consistent with the gaseous mass for this structure (0.5 km s^{-1} over a 0.1 pc scale) is 5 $M_\odot$, which is consistent with the gaseous mass seen in this experiment. What about the pattern of the kinematics? In the case of HH 1–2 (Torrelles et al. 1994), we argued that if there is a central disk or toroid, motions within the disk can be interpreted with reference to the detected outflow. If the central structure is perpendicular to the outflow, then the outflow is blueshifted in the southeast direction, suggesting that the northwestern side of the central disk must be in the foreground, as compared to the southeastern side of the central disk. The kinematics seen in Figures 7 and 8 could be consistent with a slowly contracting and rotating structure. That the velocity features appear to be distinct, and that the velocity gradient between HH 25–26 A and HH 25–26 B seems to be fairly steep (Fig. 7), could be due to the fact that the structure is more or less like a toroid in which the central part has been evacuated (Fig. 3*b*). The velocity gradient in the northeast-southwest (major axis) direction would correspond to rotation. The velocity gradient in the southeast-northwest (minor axis) direction would correspond to contraction. What about the heating pattern? The central exciting source, if coincident with the location of the 1.3 cm continuum and 2 μm point emission, appears to be displaced toward the northeast with respect to the central cavity (Fig. 5). This suggests that the exciting source could be at the edge of a central hole. The heating might therefore be expected to be asymmetrical, with HH 25–26 A being closer and therefore more heated. The central part of HH 25–26 B is also heated, but less obviously. This may imply a further distance from the exciting source for this part of the toroid.

5.2. *Cavity Model*

All the observed characteristics might also be explained in a cavity model. In this scenario, the HH 25–26 region could be the manifestation of the interaction between a dense cloud and a young star that has formed close to the surface. The exciting source would have excavated and scraped material from the surface of the cloud inclined with respect to the plane of the sky (Fig. 11, *left*). The gas closer to the source would be pushed away and compressed, producing an expanding cavity in the cloud (Fig. 11, *right*). The exciting source could be the 1.3 cm continuum source (Fig. 6), detected midway between HH 25 and HH 26. The compressed gas composing the walls of the cavity ($M \sim 7$ $M_\odot$) would be that detected by our interferometric observations, while the extended ammonia emission ($M > 20$–70 $M_\odot$; Matthews & Little 1983, Torrelles et al. 1983), seen by the single dish, would be the original cloud. This model, has no requirement on a collimated outflow but does require it to be projected against complementary cloud structures, in

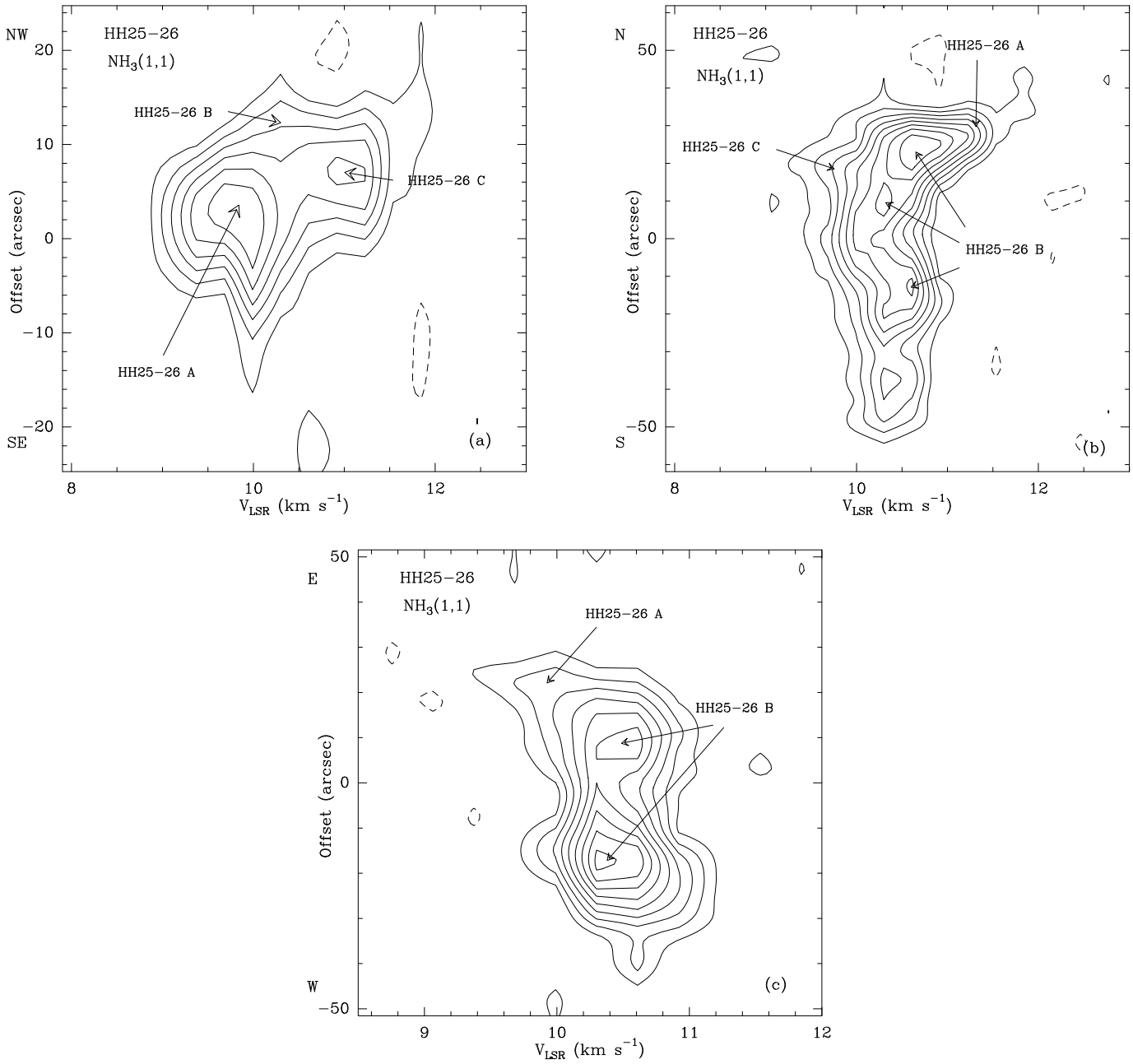

FIG. 8.—(*a*) Position-velocity diagram of $NH_3(1, 1)$ obtained across the line marked as *a* in Fig. 7. Offsets in the vertical axis are referred to the position marked with a cross in Fig. 7. Levels: −16, 16, 32, 48, 64, 80, and 96 mJy beam^{-1} (1 σ = 8 mJy). The velocity window covers the main line of the $NH_3(1, 1)$ emission. The map has been produced with natural weighting and a Gaussian tapering function of 20 kλ (beam size 9.″0 × 8.″5, P.A. = −5°). (*b*) Same as (*a*), but for the cut marked as *b* in Fig. 7. Levels: −16, 16, 32, 48, 64, 80, 96, 112, and 128 mJy beam^{-1}. (*c*) Same as (*a*), but for the cut marked as *c* in Fig. 7. Levels −16, 16, 32, 48, 64, 80, 96, 112, 128, and 144 mJy beam^{-1}.

order to explain the overlapping of the blue lobe and our VLA-NH_3 structure. The higher concentration of gas to the east could be bounding the blue outflow lobe and producing its smaller size.

We expect the outflow to sweep and disrupt the gas. The consequences should show up as perturbations in morphology, kinematics, or heating of the gas. Characteristics of this model can be identified with our results. We show in Figure 12 an overall scheme of HH 25–26, showing the relative distribution of HH 25–26 A, B, and C, the molecular outflow, and the sources present in the area.

The peak of the 1.3 cm continuum emission, and that of the associated 2 μm point feature, which shows a jetlike structure aligned with the molecular outflow (Fig. 12), is located on the edge of a cavity in the NH_3 clump. This cavity, excavated in HH 25–26 B, has enhanced rotational temperatures (§ 4.2) and infrared emission, together with illuminated edges (reflection nebulae S2, S3, and S6) ahead of the continuum source. Disruption of the dense gas may account for a gap in the border of the cavity itself, seen both in the ammonia and the reflected emission (Fig. 3*b*). The missing gas could have been radially pushed toward the south direction, producing the filament marked in the figure. This could be the case also for the other filaments observed (Figs 3*a* and 3*b*). For a previously filled cavity, the excavated mass would be $\sim 1\ M_\odot$, on the order of that

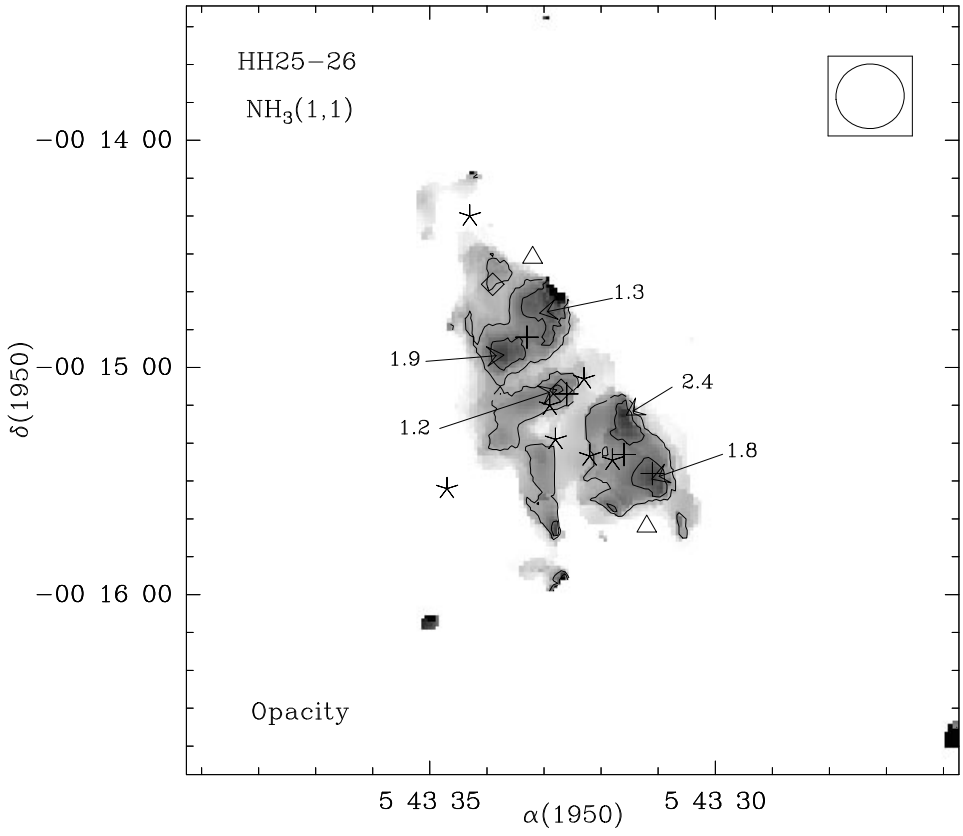

FIG. 9.—Contour map and gray-scale map of the opacity $\tau(1, 1; m)$. It has been derived as $S_\nu(1, 1; m)/S_\nu(1, 1; is) = (1-e^{-\tau(1,1;m)})/(1 - e^{-\tau(1,1;m)\times 0.28})$ (Ho & Townes 1983). The ratio $S_\nu(1, 1; m)/S_\nu(1, 1; is)$ has been approximated by the ratio of the integrated emission over the velocity range (8.4, 11.8) km s^{-1} for the main line and (1.7, 3.8) + (14.9, 18.9) km s^{-1} for the inner satellites. The contour levels correspond to an opacity of 0.2 and 1.2, and values toward the peaks have been marked in the figure. The map has been produced with natural weighting and an HPBW for the Gaussian tapering function of 20 kλ (beam size 9.″0 × 8.″5, P.A. = −5°). The marked objects are listed in Table 1.

estimated by Gibb & Heaton for the molecular outflow. The outflow could therefore consist of gas previously located within the cavity.

Assuming pressure equilibrium at a radius R between the stellar wind and the molecular gas, with volume mass density $\rho = 2m_h n(H_2)$, and velocity dispersion in one direction σ_r, we have $\dot{M}_\odot V_w/4\pi R^2 = \rho\sigma_r^2$. For a stellar wind momentum rate of 2×10^{-4} $M_\odot$ km s^{-1} yr^{-1} (Gibb & Heaton 1993), and adopting $R = 0.04$ pc (the projected physical separation between the 1.3 cm source and the edge of the cavity) and $\sigma_r = 0.6$ km s^{-1} (ammonia line width), we require a hydrogen volume density of $n(H_2) \sim 10^5$ cm^{-3}. This value is consistent with the value derived from the hydrogen column density, and therefore a stellar wind from the 1.3 cm source should be able to excavate a cavity of the observed size. We hasten to caution that the order-of-magnitude estimate is very rough because of geometrical considerations.

The kinematics of the cavity is compatible with the existence of an expanding cavity (see § 3.3 and Figs. 8*b*–8*c*). The blueshifted motions of the cavity are projected against the blue outflow lobe. The momentum of HH 25–26 A, B, and C is ~ 4 $M_\odot$ km s^{-1}, of the same order as in the southern outflow as estimated by Gibb & Heaton (1993), ~ 3 $M_\odot$ km s^{-1}. Therefore, it cannot be ruled out that the dense clumps are expanding and beginning to be incorporated into the molecular outflow. A scheme of the kinematics of the shells is shown in Figure 11 (*right*). The large number of column density peaks and velocity features could be consistent with a large perturbation in the dense gas produced by the molecular outflow.

Enhanced rotational temperatures seen toward the interface between the NH_3 condensations could be the channels through which the outflow is being pushed, and in which the strongest heating might be expected. As mentioned above, the walls of the cavity also show enhanced temperatures.

5.3. *The Herbig-Haro Objects*

The existence of HH 25 and HH 26 is difficult to explain in either the disk or cavity model. The primary difficulty is that the HH objects are nearly perpendicular to the axis of the molecular outflow. Given the presence of the 3.6 cm continuum source detected by Anglada et al. and the possible 1.3 cm exciting source detected in this experiment, there may be a number of young stellar objects in this region. The simplest explanation for the HH objects may be multiple outflows in the region.

5.4. *Contraction or Expansion*?

Without information on the physical location of the gas along the line of sight, it is always difficult to distinguish between expansion and contraction motions. In the case of HH 25–26, the key lies in the assumption of whether the NH_3 structure lies parallel or perpendicular to the outflow. If the NH_3 gas is more or less situated along the outflow direction, then the kinematics suggest that the motion is expansion, with material being swept along by the out-

TABLE 2A

ROTATIONAL TEMPERATURES TOWARD HH 25–26 A

Positions[a]	Comments	$S_\nu(1, 1; m)$ (mJy beam^{-1})	$S_\nu(2, 2; m)$ (mJy beam^{-1})	$\tau(1, 1; m)$[b]	T_{rot}[c] (K)
05 43 33.57, −00 14 36.0	Northern area	28	21	0.6[d]	25
05 43 33.77, −00 14 38.0	Northern area	43	30	0.6[d]	24
05 43 34.10, −00 14 36.0	Northern area	54	21	0.6[d]	18
05 43 34.03, −00 14 45.0	Central area	65	22	0.7	16

[a] Listed are right ascension, in units of hours, minutes, and seconds, and declination, in units of degrees, arcminutes, and arcseconds.
[b] Opacity derived from the $S_\nu(1, 1; m)/S_\nu(1, 1; is)$.
[c] Rotational temperature derived from the ratio $T_B(2, 2; m)/T_B(1, 1; m)$ (Ho & Townes 1983).
[d] The 3 σ value, as an upper limit of the emission, is indicated.

TABLE 2B

ROTATIONAL TEMPERATURES TOWARD HH 25–26 B

Positions[a]	Comments	$S_\nu(1, 1; m)$ (mJy beam^{-1})	$S_\nu(2, 2; m)$ (mJy beam^{-1})	$\tau(1, 1; m)$[b]	T_{rot}[c] (K)
05 43 34.00, −00 14 33.2	Northern area	≤ 16[d]	17	0.6[e]	35
05 43 33.10, −00 14 46.9	Northern area	67	33	0.5	20
05 43 32.66, −00 15 22.2	Cavity (eastern edge)	31	26	0.6[e]	28
05 43 31.27, −00 15 26.2	Cavity (southern edge)	69	28	0.5	18
05 43 33.39, −00 15 22.0	Southeastern area	47	≤ 16[d]	0.6[e]	≤ 16

[a] Listed are right ascension, in units of hours, minutes, and seconds, and declination, in units of degrees, arcminutes, and arcseconds.
[b] Opacity derived from the ratio $S_\nu(1, 1; m)/S_\nu(1, 1; is)$.
[c] Rotational temperature derived from the ratio $T_B(2, 2; m)/T_B(1, 1; m)$ (Ho & Townes 1983).
[d] The 3 σ value, as an upper limit of the emission, is indicated.
[e] The satellite emission $S_\nu(1, 1; is)$ is below 3 σ. For this reason, we assume for the opacity the mean value 0.6.

TABLE 2C

ROTATIONAL TEMPERATURES TOWARD HH 25–26 C

Positions[a]	$S_\nu(1, 1; m)$ (mJy beam^{-1})	$S_\nu(2, 2; m)$ (mJy beam^{-1})	$\tau(1, 1; m)$	T_{rot}[c] (K)
05 43 33.90, −00 14 37.2	38	20	0.6[d]	20

[a] Listed are right ascension, in units of hours, minutes, and seconds, and declination, in units of degrees, arcminutes, and arcseconds.
[b] Opacity derived from the ratio $S_\nu(1, 1; m)/S_\nu(1, 1; is)$.
[c] Rotational temperature derived from the ratio $T_B(2, 2; m)/T_B(1, 1; m)$ (Ho & Townes 1983).
[d] The satellite emission $S_\nu(1, 1; is)$ is below 3 σ. For this reason, we assume for the opacity the mean value 0.6.

TABLE 3

CONDENSATIONAL PARAMETERS

Condensation	Angular Size[a] l_a(arcmin) × l_b	Physical Size l_a(pc) × l_b	$\tau(1, 1; m)$[b]	$\int S_\nu(1, 1; m)dv$[c] (Jy km s^{-1})	T_{ex}[d] (K)	$T_{rot}(2, 2; 1, 1)$[e] (K)	$N(H_2)$[f] (10^{22} cm^{-2})	$n(H_2)$[g] (10^4 cm^{-3})	M[h] ($M_\odot$)
HH 25–26 A	0.4 × 0.3	0.05 × 0.04	0.1	0.1	18	≤ 19	2.5	1.8	0.3
HH 25–26 B1[i]	0.7 × 0.4	0.00 × 0.06	1.8	1.0	7	15	2.0	8.8	2.0
HH 25–26 B2[j]	0.6 × 0.4	0.08 × 0.05	2.5	0.7	7	≤ 10	2.1	1.1	1.7
HH 25–26 B3[k]	0.7 × 0.6	0.09 × 0.09	0.1	1.3	10	15	4.1	1.5	1.2
HH 25–26 C	1.4 × 0.5	0.19 × 0.06	0.7	1.3	10	14	6.5	2.0	1.6

[a] Size of the emission at the 2 σ level.
[b] Optical depth derived from the ratio $T_B(1, 1; m)/T_B(1, 1; is)$ (Ho & Townes 1983), at the peak position of the integrated emission of each condensation.
[c] Integrated flux in the velocity range −13.2 to −8.5 km s^{-1} over the total surface of each condensation, and corrected for the primary beam response.
[d] Excitation temperature obtained from the radiative transfer equation, assuming a filling factor of 1 at the peak position of the integrated emission of each condensation.
[e] Rotational temperature obtained from the ratio $T_B(2, 2; m)/T_B(1, 1; m)$ (Ho & Townes 1983) for the peak position of the integrated emission of each condensation.
[f] Hydrogen column density derived from $[N(H_2)/\text{cm}^{-2}] \simeq 4 \times 10^{21}[\tau/(1 - e^{-\tau})] \int [T_B/K][dv/\text{km s}^{-1}]$, with T_B the brightness temperature of the NH_3 emission, T_{ex} = 13–20 K and $[NH_3/H_2] = 1 \times 10^{-8}$ (Herbst & Klemperer 1973), and with a beam of 5.″3.
[g] Hydrogen volume density derived from $n(H_2) = N(H_2)/l$, where $l = (l_a l_b)^{1/2}$.
[h] Mass derived from $[M/M_\odot] = A[\tau/(1 - e^{-\tau})][D/725 \text{ pc}]^2 \int S_\nu/\text{Jy}][dv/\text{km s}^{-1}]$, with $A \simeq 1.4$ for the obtained range in T_{ex}.
[i] Subclump of HH 25–26 B centered at $\alpha(1950)$ = 05 43 33.4 and $\delta(1950)$ = −00 14 43.0.
[j] Subclump of HH 25–26 B centered at $\alpha(1950)$ = 05 43 33.7 and $\delta(1950)$ = −00 15 14.0.
[k] Subclump of HH 25–26 B centered at $\alpha(1950)$ = 05 43 31.5 and $\delta(1950)$ = −00 15 26.0.

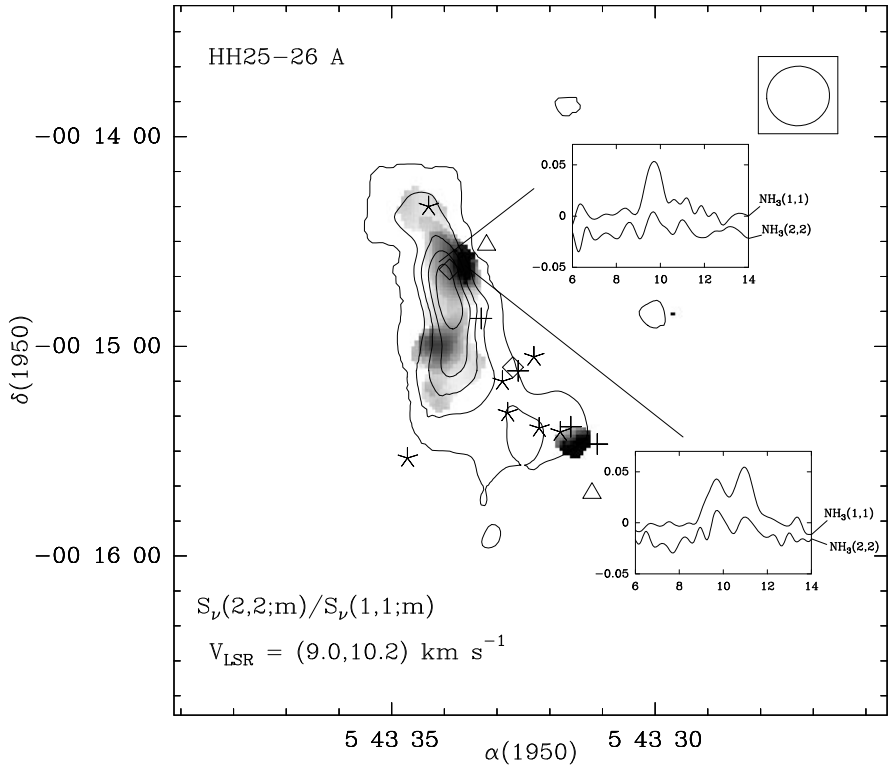

FIG. 10*a*

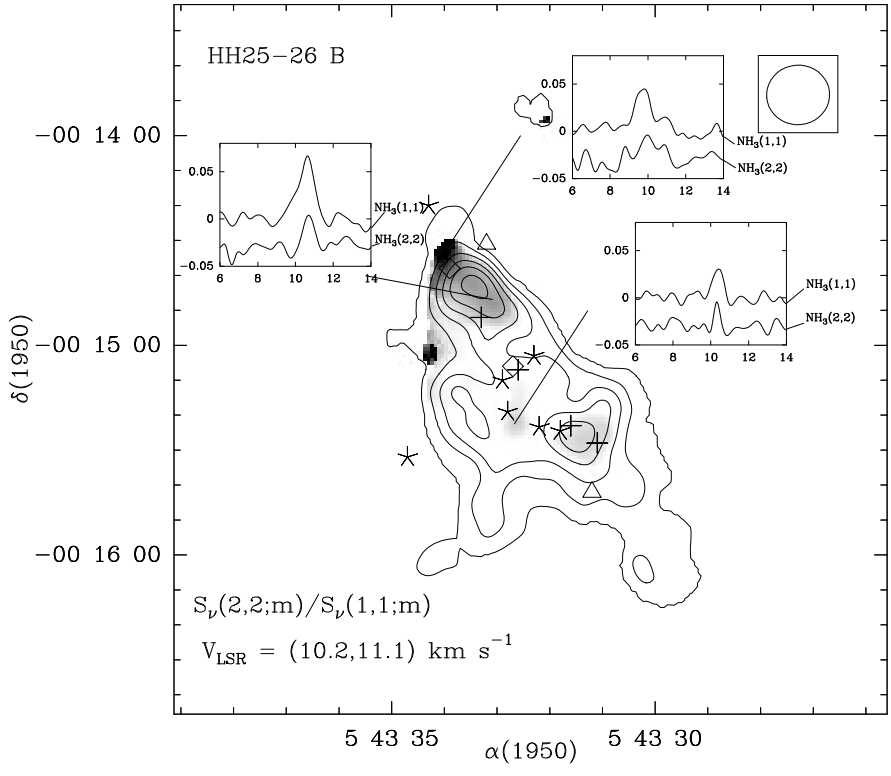

FIG. 10*b*

FIG. 10.—(*a*) Gray-scale map of the ratio $S_\nu(2, 2; m)/S_\nu(1, 1; m)$ integrated over the velocity range $(V_{LSR}/\text{km s}^{-1}) = (9.0, 10.2)$ km s^{-1}. White is 0, and black is 0.6. It has been overlapped to the emission of the (1, 1) line (see Fig. 3*a*). The map has been produced with natural weighting and an HPBW for the Gaussian tapering function of 20 kλ (beam size $9''.0 \times 8''.5$, P.A. $= -5°$). Dots mark the positions listed in Table 1. (*b*) Same as (*a*), but for $(V_{LSR}/\text{km s}^{-1}) = (10.2, 11.1)$ km s^{-1}. White is 0, and black is 0.6. (*c*) Same as (*a*), but for $(V_{LSR}/\text{km s}^{-1}) = (11.1, 11.7)$ km s^{-1}. White is 0, and black 0.5.

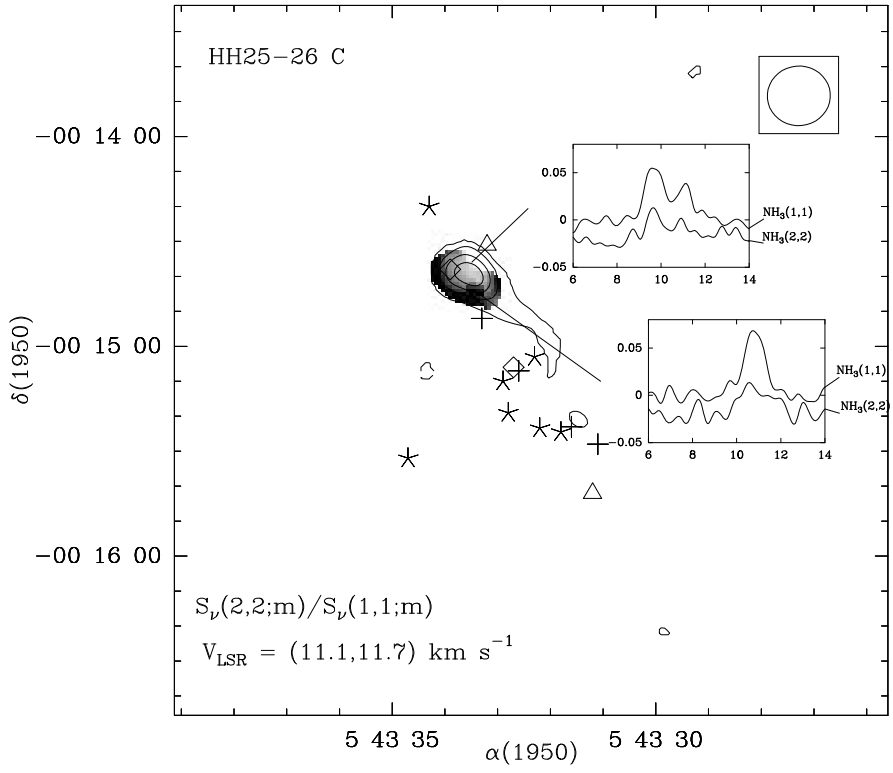

FIG. 10*c*

flowing gas. If the NH_3 gas is perpendicular to the outflow, then the kinematics suggest that contraction may be important just as in the cases like HH 1–2 or HL Tau. The motions along the minor axis together with the geometrical arrangements in all these cases suggest that the rotating disks are contracting also.

L. V-M. acknowledges the hospitality offered by the Harvard-Smithsonian Center for Astrophysics, where part of the preparation of this paper was made. L. V-M. is partially supported by SEUI (Spain) grant PB93-0159 and Junta de Andalucía (Spain). P. T. P. H. is supported in part by a NASA grant NAGW-3121.

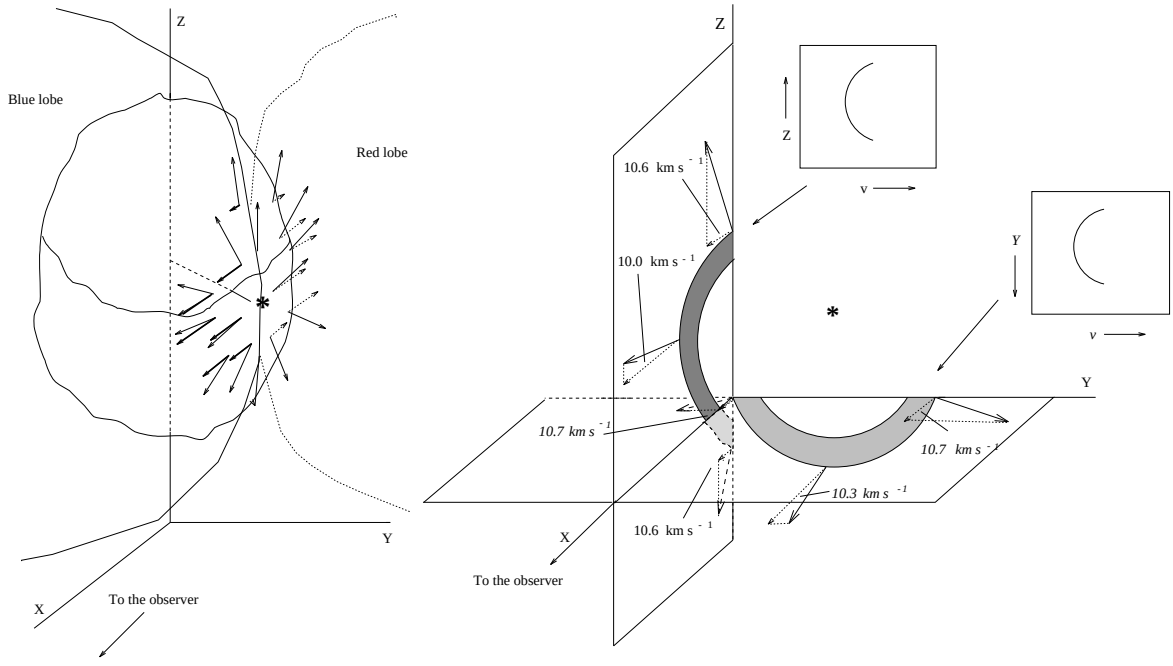

FIG. 11.—*Left*: We assume the exciting source in front of a molecular cloud, with the line joining the source and the cloud inclined with respect to the plan of the sky (*y*-*z*). The material excavated from the surface of the cloud would project as blue- and redshifted gas without needing a collimating agent. *Right*: The star has produced a cavity in the molecular cloud, as seen in Fig. 3*b*. The kinematics of its walls is schematized in this figure. Expanding shells in the *x*-*y* and *y*-*z* planes would produce the position-velocity diagrams here schematized and observed as shown in Figs. 8*b* and 8*c* when seen from the point of view of an observer located in the *x*-axis direction.

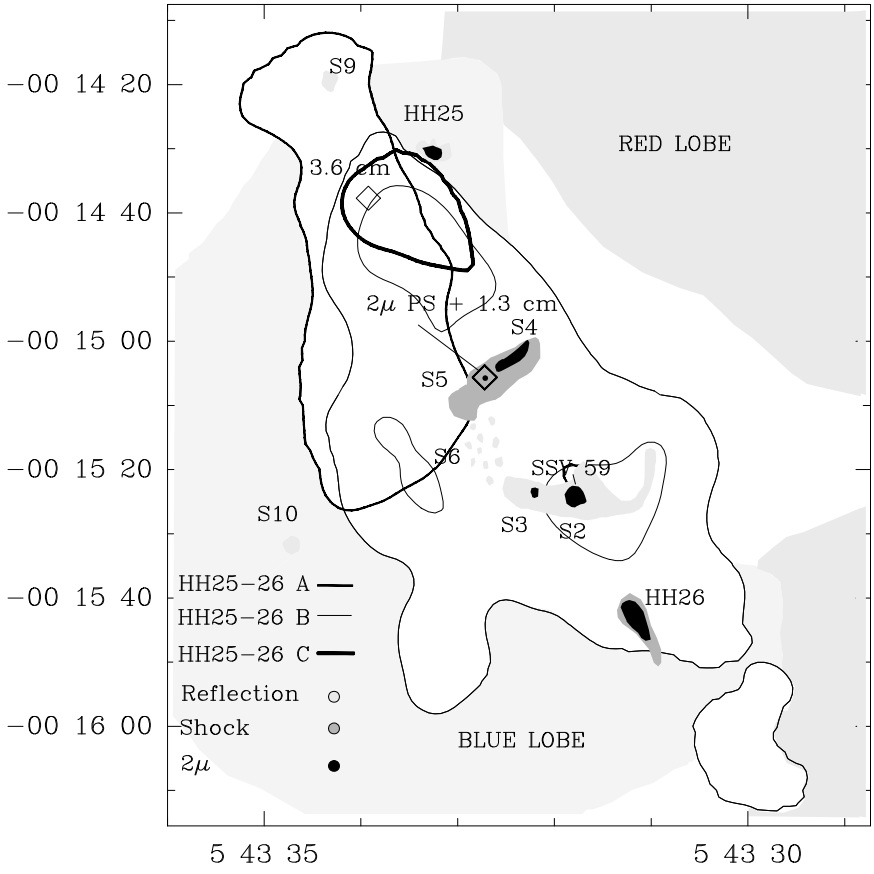

FIG. 12.—Overall scheme of our NH_3 observations together with the existent objects and molecular outflow. The boundary lines of HH 25–26 A, B, and C are marked with lines of different thickness. The CO(2–1) outflow mapped by Gibb & Heaton (1993) with 15″ of angular resolution is defined by the large gray filled areas. The smaller filled areas correspond to the main knots of emission observed in Fig. 26 from Strom et al. (1986). The darkest ones are mainly reflected light, and the lighter ones have a shocked component. The 2.2 μm emission, taken from Cohen & Schwartz (1983), is also shown as black areas.

REFERENCES

Anglada, G., et al. 1995, Rev. Mexicana Astron. Astrofis., 1, 67
Cohen, M., & Schwartz, R. D. 1983, ApJ, 265, 877
Danby, G., Flower, D. R., Valiron, P., Schilke, P., & Walmsley, C. M. 1988, MNRAS, 235, 229
Gibb, A. G., & Heaton, B. D. 1993, A&A, 276, 511
Herbst, E., & Klemperer, W. 1973, ApJ, 185, 505
Ho, P. T. P., & Townes, C. H. 1983, ARA&A, 21, 239
Matthews, N., & Little, L. T. 1983, MNRAS, 205, 123
Menten, K. M., Walmsley, C. M., & Mauersberger, R. 1987, in Circumstellar Matter, ed. I. Appenzeller & C. Jordan (Dordrecht: Reidel), 179
Pastor, J., Estalella, R., López, R., Anglada, G., Planesas, P., & Buj, J. 1991, A&A, 252, 320
Reipurth, B., Chini, R., Krügel, E., Kreysa, E., & Sievers, A. 1993, A&A, 273, 221
Snell, R. L., & Edwards, S. 1982, ApJ, 259, 668
Strom, K. M., Strom, S. E., & Vrba, F. J. 1976, AJ, 81, 308
Strom, K. M., Strom, S. E., Wolff, S. C., Morgan, J., & Wenz, M. 1986, ApJS, 62, 39
Torrelles, J. M., Goméz, J. F., Ho, P. T. P., Rodríguez, L. F., Anglada, G., & Cantó, J. 1994, ApJ, 435, 290
Torrelles, J. M., Ho, P. T. P., Rodríguez, L. F., Cantó, J., & Verdes-Montenegro, L. 1989, ApJ, 346, 756
Torrelles, J. M., Rodríguez, L. F., Cantó, J., Carral, P., Marcaide, J., Moran, J. M., & Ho, P. T. P. 1983, ApJ, 274, 214
Walmsley, C. M., & Ungerechts, H. 1983, A&A, 122, 164